Title

Free-breathing, non-ECG, simultaneous myocardial T1 , T2 , T2 *, and fat-fraction mapping with motion-resolved cardiovascular MR multitasking.

Journal

Magnetic Resonance in Medicine, 88(4)

Authors

Cao, Tianle
Wang, Nan
Kwan, Alan
et al.

Publication Date

2022-10-01

DOI

10.1002/mrm.29351

Peer reviewed

HHS Public Access

Author manuscript

Magn Reson Med. Author manuscript; available in PMC 2023 October 01.

Published in final edited form as:

Magn Reson Med. 2022 October ; 88(4): 1748–1763. doi:10.1002/mrm.29351.

Free-breathing, non-ECG, simultaneous myocardial T1, T2, T2*, and fat-fraction mapping with motion-resolved cardiovascular magnetic resonance Multitasking

Tianle Cao[1,2], **Nan Wang**[3], **Alan C. Kwan**[1,4], **Hsu-Lei Lee**[1], **Xianglun Mao**[1], **Yibin Xie**[1], **Kim-Lien Nguyen**[1,2,6], **Caroline M. Colbert**[6,7], **Fei Han**[8], **Pei Han**[1,2], **Hui Han**[1,2], **Anthony G. Christodoulou**[1,2], **Debiao Li**[1,2,*]

[1]Biomedical Imaging Research Institute, Cedars-Sinai Medical Center, Los Angeles, California, USA

[2]Department of Bioengineering, University of California, Los Angeles, Los Angeles, California, USA

[3]Radiology Department, Stanford University, Stanford, California, USA

[4]Department of Imaging and Cardiology, Cedars-Sinai Medical Center, Los Angeles, California, USA

[6]David Geffen School of Medicine and VA Greater Los Angeles Healthcare System, Los Angeles, California, USA

[7]Physics and Biology in Medicine, University of California, Los Angeles, Los Angeles, California, USA

[8]Siemens Medical Solutions USA, Inc., Los Angeles, California, USA

Abstract

Purpose: To develop a free-breathing, non-ECG technique for simultaneous myocardial T1, T2, T2*, and fat-fraction (FF) mapping in a single scan.

Methods: The MR Multitasking framework is adapted to quantify T1, T2, T2*, and FF simultaneously. A variable T_R (VTR) scheme is developed to preserve temporal resolution and imaging efficiency. The underlying high-dimensional image is modeled as a low-rank tensor, which allows accelerated acquisition and efficient reconstruction. The accuracy and/or repeatability of the technique were evaluated on static and motion phantoms, 12 healthy volunteers, and 3 patients by comparing to the reference techniques.

Results: In static and motion phantoms, T1/T2/T2*/FF measurements showed substantial consistency (R > 0.98) and excellent agreement (ICC > 0.93) with reference measurements. In human subjects, the proposed technique yielded repeatable T1, T2, T2*, and FF measurements that agreed with those from references.

*Correspondence to: Debiao Li, PhD, Biomedical Imaging Research Institute, Cedars-Sinai Medical Center, 8700 Beverly Blvd, PACT 400, Los Angeles, CA 90048, USA. debiao.li@cshs.org.

Conclusion: The proposed free-breathing, non-ECG, motion-resolved Multitasking technique allows simultaneous quantification of myocardial T1, T2, T2*, and FF in a single 2.5-min scan.

Keywords

cardiac MRI; MR Multitasking; multi-parametric mapping; free-breathing; tissue characterization

1. Introduction

Quantitative parametric mapping has gained increasing interest and attention in the clinical practice of cardiovascular magnetic resonance imaging (MRI) because of its ability to provide insight into causes of non-ischemic and ischemic cardiomyopathies as well as its potential promise to elucidate disease processes involving the myocardial microvasculature. Quantification provides an objective assessment of disease progress (1,2) and is sensitive to mild or diffuse tissue alterations (3,4). Parametric mapping of T1 and T2 is capable of detecting fibrosis (5,6), edema (7–9), whereas T2* mapping quantifies cardiac iron concentration, which is essential for evaluating β-thalassemia major and sickle cell anemia (10–12). Myocardial fat content is associated with heart failure (13) and is of high prevalence in chronic myocardial infarction (14) and nonischemic cardiomyopathies (15) such as arrhythmogenic right ventricular dysplasia.

Several mapping techniques have previously been used for myocardial characterization, including T1 mapping using Modified Look-Locker inversion recovery (MOLLI) (16) or saturation recovery single-shot acquisition (SASHA) (17), T2 mapping with T2-prepared balanced SSFP (18), and T2* mapping with multi-echo gradient recalled echo (GRE) (12). However, these methods must be used with breath-holding and electrocardiogram (ECG) triggering to minimize respiratory and cardiac motion effects. Furthermore, separate acquisitions are needed for mapping separate parameters, resulting in potential misaligned maps and variable breath-holding quality.

Free-breathing techniques for cardiac parametric mapping have been developed using respiratory gating (19–21), bellows (22) or respiratory self-navigation signals (23,24). However, respiratory gating is inefficient and can lead to long and unpredictable scan time, as data is only acquired in short windows dependent on individual subject motion. Bellows only provide a relative measure of respiratory motion rather than an absolute measure of diaphragmatic motion, which can lead to errors in respiratory motion identification (25). Respiratory self-navigation can address some of these issues but does not reach 100% acquisition efficiency unless it is also paired with cardiac self-navigation. The above mapping techniques all rely on less-efficient ECG gating, which is prone to errors at high field strengths (26) and for patients with arrhythmia (27).

Free-breathing, non-ECG cardiac T1 and T2 mapping has been achieved using the MR Multitasking framework (28,29), which models the underlying image as a low-rank tensor and acquires training data to identify and resolve cardiac and respiratory motion. However, this framework has yet to include T2* and fat fraction (FF) mapping in the heart. Multi-echo extensions of Multitasking for T1, T2, and T2* mapping in the brain (30) and T1, R2*, and FF mapping in the liver (31) have been described. However, adding multiple echoes

after every excitation pulse comes at the price of prolonged scan time and reduced temporal resolution, limiting the direct translation of these multi-echo extensions to cardiac imaging.

To address several limitations of prior techniques and to tailor the multitasking framework for multiparametric myocardial mapping, we developed a new technique based on MR Multitasking for the joint mapping of myocardial T1, T2, T2*, and FF from a free-breathing, non-ECG triggered, 2D single slice acquisition. This technique includes (1) hybrid T2prep/IR (T2IR) preparations and multi-echo readouts to sample T1, T2, and T2* relaxations; (2) a variable T_R (VTR) scheme alternating between single-echo and multi-echo readouts, for improved temporal resolution and shorter scan time; (3) low-rank tensor (LRT) modeling to reconstruct the underlying images; and (4) a chemical-shift based method (32) for water and fat separation. The performance of the proposed technique was evaluated on phantom, healthy volunteers, and patients with ferumoxytol enhancement.

2. Methods

2.1 Imaging framework

2.1.1 Sequence diagram—The sequence diagram used in this work is shown in Figure 1A. The acquisition cycles through hybrid T2IR modules with five different preparation durations ($\boldsymbol{\tau}$, with $\boldsymbol{\tau} = 0$ corresponding to a standard IR pulse), with FLASH excitations for data readout filling the entire recovery period between preparation pulses. Two interleaved datasets are collected during the continuous acquisition: the training data ($\mathbf{d}_{\mathrm{tr}}$) are frequently collected at k-space center (0° radial spoke) to provide temporal information; the imaging data ($\mathbf{d}_{\mathrm{img}}$) are collected with golden-angle radial trajectory to provide spatial information. In previous MR Multitasking work for T2* mapping (30,31), multi-echo readouts were used for both training and imaging data (Figure 1B), which limited the temporal resolution and imaging efficiency. To achieve a higher temporal resolution to characterize cardiac motion, instead of using constant T_R (CTR) for both datasets, a variable T_R (VTR) scheme was developed in this work, where the training data are collected using a single-echo, short T_R readout and imaging data are collected using a multi-echo, long T_R readout (Figure 1C).

2.1.2 Low-rank tensor imaging model—The MR Multitasking framework models the underlying image as a 7D image $x(\mathbf{r}, T_c, T_r, \tau, T_I, T_E)$ with two spatial dimensions indexed by $\mathbf{r} = [x, y]$, and five temporal dimensions describing cardiac motion, respiratory motion, T2 preparation, T1 recovery, and gradient echo dynamics (T2* decay and fat–water shift), indexed by T_c, T_r, τ, T_I, and T_E, respectively. By taking advantage of the spatial-temporal correlations (33), the image can be factorized as:

$$x(\mathbf{r}, T_{\mathrm{c}}, T_{\mathrm{r}}, \tau, T_I, T_E) = \sum_{\ell=1}^{L} u_\ell(\mathbf{r})\phi_\ell(T_{\mathrm{c}}, T_{\mathrm{r}}, \tau, T_{\mathrm{I}}, T_{\mathrm{E}}), \quad (1)$$

$$\phi_\ell(T_{\mathrm{c}}, T_{\mathrm{r}}, \tau, T_{\mathrm{I}}, T_{\mathrm{E}}) = \sum_{j=1}^{J}\sum_{k=1}^{K}\sum_{m=1}^{M}\sum_{n=1}^{N}\sum_{p=1}^{P} g_{\ell jkmnp} c_j(T_{\mathrm{c}}) r_k(T_{\mathrm{r}}) v_m(\tau) w_n(T_{\mathrm{I}}) q_p(T_{\mathrm{E}}), \quad (2)$$

where $\{u_\ell(\mathbf{r})\}_{\ell=1}^{L}$ represent spatial coefficients and $\{(\phi_\ell(T_c, T_r, \tau, T_I, T_E)\}_{\ell=1}^{L}$ represent temporal functions which can be further decomposed into a core tensor $\mathcal{G}$ with elements $g_{\ell jkmnp}$ and individual bases for each temporal dimension: $\{c_j(T_c)\}_{j=1}^{J}$, $\{r_k(T_r)\}_{k=1}^{K}$, $\{v_m(\tau)\}_{m=1}^{M}$, $\{w_n(T_\mathrm{I})\}_{n=1}^{N}$, and $\{q_p(T_\mathrm{E})\}_{p=1}^{P}$ (34). The combination of Eqs. (1) and (2) suggests that a discretized image tensor $\mathcal{X}$ with elements $x_{ijkmnp} = x(\mathbf{r}_i, T_{\mathrm{c,j}}, T_{\mathrm{r},k}, \boldsymbol{\tau}_m, T_{\mathrm{I},n}, T_{\mathrm{E},p})$ can be decomposed in Tucker form (35,36) as follows:

$$\mathcal{X} = \mathcal{G} \times_1 \mathbf{U} \times_2 \mathbf{C} \times_3 \mathbf{R} \times_4 \mathbf{V} \times_5 \mathbf{W} \times_6 \mathbf{Q}, \tag{3}$$

where the columns of **U**, **C**, **R**, **V**, **W**, and **Q** contain the basis functions for each corresponding dimension.

In MR Multitasking, the core tensor and temporal bases are often extracted from the training data, as will be described in Section 2.1.3. However, because our VTR scheme collects only a single-echo readout for training data, multi-echo temporal information to determine **Q** and the 6$^{\mathrm{th}}$ dimension of $\mathcal{G}$ will not be available. Therefore, we instead individually decompose each tensor $\mathcal{X}_p$, the subset of the image tensor $\mathcal{X}$ at the p^{th} echo:

$$\mathcal{X}_p = \widetilde{\mathcal{G}} \times_1 \mathbf{U}_p \times_2 \mathbf{C} \times_3 \mathbf{R} \times_4 \mathbf{V} \times_5 \mathbf{W}, \tag{4}$$

where $\widetilde{\mathcal{G}}$ is an updated core tensor without a gradient-echo dimension, and $\mathbf{U}_p$ are the spatial coefficients for the pth echo. All echoes share the motion bases and T1 and T2 relaxation bases, as changes in motion and T1/T2 relaxation are negligible on the time scale between echoes.

2.1.3 Image Reconstruction—This work adopts a similar strategy for MR Multitasking image reconstruction to previously published methods (28,29,37,38). Briefly, this reconstruction workflow (1) predetermines the T1 and T2 temporal basis functions in **V** and **W** from a dictionary of signal curves, (2) reconstructs “real-time” images and perform motion binning, (3) recovers the missing elements in the training dataset, (4) estimates the cardiac basis functions in **C**, respiratory basis functions in **R**, and core tensor $\widetilde{\mathcal{G}}$ from training data, and (5) solves spatial coefficients $\mathbf{U}_p$ for each echo from imaging data.

A dictionary of feasible T2IR GRE signal curves is generated using the sequence parameters and a range of T1/T2 and B_1 inhomogeneity values based on the Bloch equations (28,29,38). The dictionary consists of 21 T1 values logarithmically spaced from 100 ms to 3000 ms, 21 T2 values logarithmically spaced from 10 ms to 3000 ms, 10 flip angles equally spaced between 0.5° to 5°, and 6 inversion efficiency factors equally spaced between −1 (perfect inversion) and −0.5. The T1 basis functions in **W** and T2 basis functions in **V** are obtained from the high-order SVD (HOSVD) (39) of the dictionary.

The second reconstruction step is to generate ungated images with an explicit low-rank matrix imaging strategy. The ‘real-time’ (ungated) temporal basis functions are estimated from singular value decomposition (SVD) of the training data. It has only one dimension

representing the elapsed acquisition time and is similar to ϕ_i in Eq. (1). The spatial coefficients can therefore be estimated through a least-squares fitting to the imaging data.

A modified k-means clustering algorithm as previously described (28) is used to automatically place the corresponding images into 6 respiratory bins and 20 cardiac bins. To address the changing contrast weightings after the preparation pulses, the centroids solved in each iteration at different contrast combinations are constrained by the pre-determined T1/T2 bases **V** and **W**. Respiratory motion is identified first, and the respiratory bins assigned at each iteration are low-pass filtered with 50 Hz cutoff frequency. Then cardiac motion is binned with the same algorithm, expect that the cardiac bins are band-pass filtered with range of 50 – 130 Hz (a range for possible heart rates).

The training tensor $\mathscr{D}_{\text{tr}}$, as expressed in ($\mathbf{k}$, T_{c}, T_{r}, τ, T_{I})-space, can still be undersampled as training data acquisition cannot typically cover every combination of cardiac phase, respiratory phase, T2-IR prep duration, and inversion time. We apply a small-scale low-rank tensor completion algorithm by solving the optimization problem below:

$$\widehat{\mathscr{D}}_{\text{tr}} = \arg \min_{\substack{\mathscr{D}_{\text{tr}}, \text{ s.t.} \\ \mathbf{D}_{\text{tr},(4)} \in \text{range}(\mathbf{V}), \\ \mathbf{D}_{\text{tr},(5)} \in \text{range}(\mathbf{W})}} \left\| \mathbf{d}_{\text{tr}} - \Omega_{\text{tr}}(\mathscr{D}_{\text{tr}}) \right\|_2^2 + \lambda \sum_{i=1}^{3} \left\| \mathbf{D}_{\text{tr},(i)} \right\|_* + R_{\text{t}}(\mathscr{D}_{\text{tr}}), \tag{5}$$

where $\mathbf{d}_{\text{tr}}$ is the collected training data, $\Omega_{\text{tr}}(\cdot)$ is the sampling operator for the training dataset, $\mathbf{D}_{\text{tr},(i)}$ is the mode-i unfolding of the complete training tensor, $\|\cdot\|_*$ denotes the matrix nuclear norm, and $R_{\text{t}}(\cdot)$ is a temporal regularizer, which in this work is chosen as temporal total variation (TV) along the respiratory and cardiac dimensions. Once the training tensor is completed, the cardiac basis functions in **C**, respiratory basis functions in **R**, and core tensor $\widetilde{\mathscr{G}}$ can be extracted from the HOSVD of $\mathscr{D}_{\text{tr}}$.

Finally, we solve the spatial coefficients **U** echo-by-echo:

$$\widehat{\mathbf{U}}_p = \arg\min_{\mathbf{U}_p} \left\| \mathbf{d}_{\text{img},p} - \Omega\left(\widehat{\boldsymbol{\Phi}} \times_1 \mathbf{FSU}_p\right) \right\|_2^2 + \lambda R_{\text{s}}(\mathbf{U}_p), \tag{6}$$

for known temporal factor tensor $\widehat{\boldsymbol{\Phi}} = \widetilde{\mathscr{G}} \times_2 \mathbf{C} \times_3 \mathbf{R} \times_4 \mathbf{V} \times_5 \mathbf{W}$, where $\mathbf{d}_{\text{img},p}$ is the imaging data at the p^{th} echo, and $R_{\text{s}}(\cdot)$ is a wavelet sparsity regularizer. The reconstructed image tensor for the p^{th} echo is then given by the product $\widehat{\mathscr{X}}_p = \widehat{\boldsymbol{\Phi}} \times_1 \widehat{\mathbf{U}}_p$.

A flow chart for image reconstruction can be found in Supporting Information Figure S1.

2.1.4 Parameter quantification—All quantification processes are performed at the end-expiration and end-diastolic phases of the reconstructed images.

The signal equation was derived based on the sequence structure and Bloch equations, as detailed in Supporting information Section A. T1 and T2 values are fitted voxel-by-voxel from the signal equation, using the *lsqnonlin* solver in MATLAB.

T2* mapping and water-fat separation are performed jointly using the reconstructed multi-echo images of the last inversion time with the longest T2IR preparation duration, which are closest to the GRE steady state. Specifically, the following equation is solved for each multi-echo image $y(\mathbf{r}, T_E)$:

$$y(\mathbf{r}, T_E) = \left(\mathcal{W}(\mathbf{r}) + \sum_l C_l \mathcal{F}(\mathbf{r}) e^{i2\pi f_l T_E}\right) e^{if_{B0} T_E - T_E/T_2^*}, \quad (7)$$

using a graph-cut algorithm (32), where $\mathcal{W}(\mathbf{r})$ and $\mathcal{F}(\mathbf{r})$ are the water and fat components, C_l and f_l are the weightings and the resonance frequency offsets of the lth fat peak, f_{B0} (in Hz) is the local frequency shift due to static field inhomogeneity. A multi-peak fat spectrum is employed here according to previous work (40). Finally, FF in each voxel is calculated as (41):

$$FF(\mathbf{r}) = \begin{cases} \dfrac{|\mathcal{F}(\mathbf{r})|}{|\mathcal{F}(\mathbf{r}) + \mathcal{W}(\mathbf{r})|}, & \text{if} \quad \mathcal{F}(\mathbf{r}) > \mathcal{W}(\mathbf{r}) \\ 1 - \dfrac{|\mathcal{W}(\mathbf{r})|}{|\mathcal{F}(\mathbf{r}) + \mathcal{W}(\mathbf{r})|}, & \text{otherwise} \end{cases} \quad (8)$$

2.2 Data Acquisition

2.2.1 VTR Multitasking imaging parameters—VTR Multitasking acquisition cycled through hybrid T2IR modules with preparation times τ = 0, 30, 40, 50, 60 ms. Eleven echo times at T_E = 1.6 – 14.6 ms were collected for imaging data and a single echo at T_E = 1.6 ms was collected for training data. The scan time for VTR Multitasking was 2.5 min/slice. Scan parameters were: field of view (FOV) = 270 × 270 mm^2, in-plane resolution = 1.7 × 1.7 mm^2, slice thickness = 8.0 mm. More details of the imaging protocol are available in Table 1.

2.2.2 Phantom study—An ISMRM/NIST phantom (model 130, High Prevision Devices, Boulder, Colorado USA) was scanned for validation of T1 and T2. A Calimetrix phantom (Calimetrix, Madison, WI) was scanned for validating T2*. To validate FF, a separate phantom was constructed with ten vials with target fat concentrations 0%, 1%, 3%, 5%, 7%, 9%, 10%, 15%, 20%, 30%, surrounded by de-ionized water.

Inversion-recovery spin echo (IR-SE) and T2-weighted spin echo (T2-SE) were acquired as references for T1 and T2, respectively. For the T2* reference, single-echo GRE images were acquired for ten different echo times between 1 ms and 25 ms. A product q-DIXON sequence with 6 bipolar readouts was used as a reference for FF. Imaging parameters for all reference sequences are summarized in Supporting Information Table S1.

The above phantoms were put onto a linear motion stage (SHELLEY, Toronto, Ontario CANADA) to test the performance of the proposed VTR Multitasking technique to translational motion (period = 3.5 s, similar to respiratory motion). CTR Multitasking was also scanned for comparison. The phantom and the motion stage were placed as illustrated in Supporting Information Figure S2 to generate both in-plane and through-plane motion.

2.2.3 In vivo study—The in vivo study was approved by the institutional review board at Cedars-Sinai Medical Center and at VA Greater Los Angeles Healthcare System. Written informed consent from all subjects was obtained before the study. $N = 12$ healthy volunteers (age: 38.2 ± 13.1, 4 male) were recruited and scanned on a 3T scanner (MAGNETOM Vida, Siemens Healthineers, Erlangen, Germany) with a standard 18-channel body coil and an integrated spine matrix coil. VTR Multitasking acquisition was performed in short-axis views (basal, mid-ventricular, and apical slices). Reference protocols were scanned in the same imaging slices with an end-expiration breath-hold, and triggered to the end-diastolic cardiac phase. Reference sequences included MOLLI for T1 mapping and T2-prep GRE for T2 mapping. ME-GRE with 20° flip angle and 8 echo times ranging from 1.6 – 16.3 ms was used as the T2* reference (21,42). A prototype 6-point Dixon GRE sequence with 5° flip angle (43–46) was used as the FF reference. Detailed parameters are listed in Supporting information Table S2. Both VTR Multitasking and references were repeated once more at the mid-ventricular slice to test scan-rescan repeatability. Parametric maps were also acquired using CTR Multitasking (with identical scan time and parameters as VTR, except that $T_E = 1.6 – 14.6$ ms was used for both imaging and training data) at the mid-ventricular slice for comparison against VTR Multitasking.

To further validate the proposed technique on abnormal T2* values, the VTR Multitasking and reference T2* mapping sequences were incorporated as part of the clinical protocol with ferumoxytol (Feraheme, Covis Pharma, Cary, NC, USA) enhancement, which mimicked increased myocardial iron content. 3 patients (age: 70.7 ± 15.5, 2 male) with known ischemic heart diseases were scanned on a 3T scanner (MAGNETOM Skyra, Siemens Healthineers, Erlangen, Germany) with a standard 18-channel body coil and an integrated spine matrix coil. The images were acquired in the mid-ventricular slice at baseline, and following a 12-min intravenous infusion of ferumoxytol (4.0 mg/kg).

The reference T1, T2, and T2* maps were automatically generated by the scanner. The reference FF maps were computed from complex images as described in Methods Section 2.1.4.

2.3 Analysis

All reconstructions were performed using MATLAB 2016b (MathWorks, Natick, Massachusetts) on a Linux workstation with a 3.08-GHz dual 16-core Intel Xeon processor and 256 GB RAM, which took about 3.5 hours for each slice. The rank for the T1 dimension was chosen as 5 from the −40 dB threshold on the normalized singular value curves of the simulated dictionary. The ranks for T2, respiratory motion, and cardiac motion dimensions were not truncated, as the nuclear norm term in Equation (5) for training tensor completion already performed a soft constraint on the tensor ranks of those dimensions. Finally, the rank for spatial dimension was empirically set to 48. MATLAB p-code for reconstruction is available upon reasonable request.

For phantom study, T1/T2/T2*/FF measurements were calculated for each vial. Linear regression was performed for the relevant range (T1: 0–2000 ms, T2, T2*: 0–100 ms, FF: 0 – 100%) and intraclass correlation coefficients (ICCs) were calculated from a two-way

mixed model and 95% confidence using IBM SPSS Statistics (Armonk, New York) to evaluate the agreement between VTR Multitasking and the references.

A correlation analysis was performed between VTR Multitasking measurements of the motion phantom and the static reference values, between moving and static VTR Multitasking measurements, and between moving CTR and VTR Multitasking measurements. ICCs were calculated to assess agreement. SNR in each vial (defined as mean value over standard deviation) was calculated and compared between VTR and CTR measurements with Wilcoxon signed rank test.

The in vivo mid-ventricular maps of healthy subjects from different methods (references, VTR Multitasking, and CTR Multitasking) were blinded and pooled and assessed by an imaging cardiologist (A.C.K.). The T1 and T2 maps were scored based on a 4-point grading system (43): 1, uninterpretable; 2, poor (blurring and residual artifacts); 3, acceptable (mildly blurring and mild residual artifacts); 4 excellent (sharp myocardium wall and no artifact). The T2* maps were scored based on a 5-point grading system (47): 0, unusable; 1, poor (heart just visible); 2, average (with severe septal artifact) 3, good (with moderate septal artifact); 4, very good (with mild septal artifact); 5, excellent (with negligible septal artifact). FF maps were not scored due to a lack of expertise (FF quantification is not clinically performed yet). The scores from the proposed VTR Multitasking were compared to those from reference and CTR Multitasking method using Wilcoxon signed-rank test.

The in vivo reference and VTR Multitasking maps were segmented in CVI 42 (Circle Cardiovascular imaging, Calgary, Alberta, Canada) using the AHA 16-segment model (48). Specifically, the epi- and endo-cardial contours were drawn on VTR Multitasking T1 maps and were copied to other VTR Multitasking maps, which are co-registered. For reference T1 and T2 maps, the contours were drawn separately on the maps. For reference T2* and FF maps, the ROIs were traced separately on the raw images (12) and were copied to the maps. Finally, automatic segmentation was performed by the software using the contours.

The T1, T2, T2*, and FF values in the 16 myocardial segments were used for comparison between VTR Multitasking and references. Myocardial homogeneity in healthy subjects was assessed using the root-mean square (RMS) inter-segment standard deviation (ISSD), which was calculated as the standard deviation of the 16 segmental values for each subject, aggregated across subjects using RMS. Repeatability in healthy subjects was assessed using the RMS within-segment standard deviation (WSSD), which was calculated as the standard deviation of the 2 test–retest values for each segment and aggregated across segments and subjects using RMS, and coefficient of variation (CoV), which was calculated by normalizing the RMS-WSSD with the mean value of the 6 mid-ventricular segments. A 3-way ANOVA test (with methods, subject groups, pre- or post-contrast as independent variables) was performed on the mean T1/T2* measurements in each subject to test for statistically significant differences ($P<0.05$) between different methods. A two-tailed student t-test was used for comparing mean T2/FF measurements between different methods (with $P<0.05$ as significant), as these reference measurements were not available in patient groups. The agreement between different methods and between repeated measurements were assessed using Bland-Altman analysis.

3. Results

3.1 Phantom study

Phantom results shown in Figure 2A demonstrated good quality of VTR Multitasking maps both with and without motion. Substantial correlation (R = 0.998, 0.999, 0.979, and 0.995 for T1/T2/T2*/FF, respectively) and agreement (ICC = 0.990, 0.959, 0.978, and 0.991 for T1/T2/T2*/FF, respectively) were found between VTR Multitasking and reference measurements (Figure 2B). With motion, VTR Multitasking measurements still showed good correlation (R = 0.999, 0.999, 0.986, and 0.995 for T1/T2/T2*/FF, respectively) and agreed (ICC = 0.988, 0.934, 0.981, and 0.993 for T1/T2/T2*/FF, respectively) with the reference measurements (Figure 2C). Supporting Information Figure S3 plots VTR Multitasking measurements with motion against those without motion. The fitted slopes through regression analysis were 0.984, 0.980, 0.948, and 0.948 for T1/T2/T2*/FF, respectively. The correlation coefficients (R > 0.95) and ICCs (ICC > 0.96) indicated agreement.

The comparison between VTR and CTR Multitasking on motion phantoms can be found in Supporting Information Figure S4. The maps resembled each other, and the fitted slopes were 0.965, 0.926, 0.959, and 0.961 for T1/T2/T2*/FF, respectively. Their measurements were consistent, as indicated by R and ICC (R > 0.97, ICC > 0.97). The SNR comparison in each vial demonstrated significantly better T1 precision with the VTR approach (P = 0.002). No significant difference was found for other parameters (P = 0.063, 0.359, and 0.106 for T2/T2*/FF, respectively).

3.2 In vivo study

Figure 3 compares VTR and CTR Multitasking maps of 3 healthy subjects. Improved SNR and image quality are apparent on the VTR T1 and T2 maps. The white arrow on the CTR T1 map indicates myocardial artifacts produced by CTR Multitasking. T2* and FF maps from both methods appeared similar. The image quality scores for VTR and CTR Multitasking are shown in Supporting Information Figure S5, which indicated significantly higher scores for VTR T1 maps (VTR median score: 3, CTR median score: 2, P = 0.008). No significant differences were found in scores of T2 (both with median score: 3, P = 0.766) and T2* maps (VTR median score: 4, CTR median score: 3, P = 0.371).

Mapping results from a representative healthy subject are shown in Figure 4 for VTR Multitasking and references (2 more healthy subjects are shown in Supporting Information Figure S6–7). VTR Multitasking produced co-registered maps that resembled reference maps. The image quality scores in Supporting Information Figure S5 indicated significantly lower T1 scores of VTR Multitasking compared to those of MOLLI (VTR median score: 3, MOLLI median score: 4, P = 0.008). No significant differences were found for T2 (both with median score: 3, P = 1.000) and T2* maps (VTR median score: 4, reference median score: 3, P = 0.125). AHA 16-segment bullseye plots in Figure 5 show the mean quantitative measures across all 12 healthy subjects for T1, T2, T2*, and FF. Both methods demonstrated little spatial variability in T1 (RMS-ISSD < 80ms) and T2 maps (RMS-ISSD < 4 ms). Higher spatial variability relative to the mean was found on T2* maps of both methods,

both of which measured lower T2* values in the infero-lateral segment. VTR Multitasking FF maps showed better spatial homogeneity than reference maps (2.7% vs. 5.2%) and both methods indicated little-to-no myocardial fat in healthy subjects.

VTR Multitasking maps and available reference maps for a patient are shown in Figure 6. Both Multitasking and reference T2* map showed reduced T2* after ferumoxytol administration.

T1, T2, T2*, and FF measurements from VTR Multitasking and available references are shown in Table 2 for all subjects. Statistical analysis indicated small but significant differences between VTR Multitasking and references for T1 ($P = 0.001$, 3-way ANOVA) and T2 ($P<0.001$, t-test). No significant differences were found between VTR Multitasking and references for T2* ($P=0.820$, 3-way ANOVA) and FF measurements ($P=0.307$, t-test). Bland-Altman analyses in the global myocardium and in each of the 16 segments are shown in Figure 7, with the following limits of agreement: global T1: ±93 ms; global T2: ±10 ms, global T2*: ±4 ms, global FF: ±7%; segment-wise T1: ±176 ms, segment-wise T2: ±9 ms, segment-wise T2*: ±11 ms, segment-wise FF: ±12%.

Figure 8 shows repeatability measurements from VTR Multitasking and references for the mid-ventricular slice. Supporting Information Figure S8 shows Bland-Altman plots of VTR Multitasking repeated measurements in the global region and in the 6 mid-ventricular segments. The limits of agreement between first and second VTR Multitasking scan were: global T1: ±76 ms, global T2: ±3 ms, global T2*: ±7 ms, global FF: ±1%; segment-wise T1: ±181 ms, segment-wise T2: ±7 ms, segment-wise T2*: ±9 ms, segment-wise FF: ±3%). Both VTR Multitasking and references demonstrated good repeatability, as indicated by RMS-WSSD (T1: < 65 ms, T2: < 3 ms, T2*: < 4 ms, FF: < 2 %) and CoV (T1: < 6%, T2: < 7%, T2*: < 15%, FF: < 77%).

4. Discussion

Conventional single parametric cardiac mapping requires multiple breath-hold scans (16–18), leading to long scan times, potential image misregistration, and patient fatigue. Advanced techniques including 2D T1/T2/FF mapping (43) and T1/T2/T2*/FF mapping (49) with a single breath-hold and free-breathing multi-parametric mapping techniques such as 3D T1/T2 mapping (23) and 2D T1/T2/T2* mapping (21) have been developed. However, ECG signal is still required to deal with cardiac motion, which is prone to noise and errors particularly at high field strengths (26) and may fail in arrhythmia patients. In fact, a previous study (50) at 3T showed that ECG triggering failed for up to 35% of patients with regular sinus rhythm. In this work, a free-breathing, non-ECG technique was developed for simultaneous and co-registered myocardial T1, T2, T2*, and FF quantification based on the MR Multitasking framework. The technique was validated on static and motion phantoms, healthy volunteers, and patients, and the results indicated that the technique could provide repeatable measurements that agreed with the references.

CTR Multitasking using multi-echo readouts and a constant T_R for both training and imaging data has been recently presented for T2* mapping in the brain (30) and T2*/FF

mapping in the liver (31). The VTR approach proposed in this work clearly outperformed the CTR approach in motion phantoms and in the heart, as shown in Figure 3 and Supporting Information Figure S4–5. Potential reasons include: (a) VTR collects more imaging data than CTR per unit scan time, resulting in improved imaging efficiency. (b) VTR has a higher temporal resolution (i.e., frequency of training data collection). With a T_R of 16 ms, the temporal resolution of the CTR approach will be at least 32 ms, thus making it more challenging to perform cardiac motion binning. In contrast, the temporal resolution of VTR in this work improved to 20 ms.

The VTR Multitasking measurements in phantoms were in good agreement with the SE and GRE references, yet T1 and T2 underestimation was observed. One possible cause of T1 underestimation could be magnetization transfer effect (51). T2 underestimation could potentially be caused by the sensitivity of the VTR Multitasking preparation scheme (T2IR) to B_1 inhomogeneity (52). The VTR Multitasking measurements in moving phantoms showed similar results, which demonstrated the robustness of our technique to in-plane and through-plane motion. There were differences between the VTR Multitasking T2* measurements with and without motion (especially the penultimate vial), which could be related to B_0 field changes during phantom movement.

The in vivo VTR Multitasking maps showed good spatial homogeneity, especially in T1 and T2. Both VTR Multitasking and reference methods revealed relatively low T2* values in the infero-lateral segment, resulting in higher relative spatial variability in T2* maps. Both techniques also showed lower T2* repeatability around the lateral wall than in other segments. This may be related to susceptibility artifacts around tissue boundaries, leading to less reliable T2* measurement for both the Multitasking and reference techniques (53,54). This has been a common issue for T2* mapping especially at high fields, and our technique performed similarly to the conventional ones in this aspect.

In addition to the T2 differences between VTR Multitasking and references as in the phantom study, the statistical test also showed a small but significant difference in T1 measurements. One possible explanation would be T1 underestimation from MOLLI due to magnetization transfer, T2 confounding factors, and dependence on heart rate (51). The potential mismatch between cardiac phases and respiratory phases during analysis may partially contribute to these differences as well. In Multitasking, the cardiac phase with largest blood pool was selected as diastole and the respiratory phase with highest liver position was selected as end-expiration. In reference scans, however, the acquired phase may not always be diastole due to heart rate variations and breath-holding positions may vary based on given durations for exhalation. Despite the differences, VTR Multitasking measurements in healthy volunteers were still within or close to previous literature range at 3T (T1: 1100–1314 ms, T2: 38–46 ms, T2*: 20.5 – 24 ms, FF: 1–1.5 %) (42,43,47,55–58). The repeatability of Multitasking T1 measurements (RMS-WSSD: 65 ms) were lower than that of MOLLI (RMS-WSSD: 27 ms), yet the variance in T1 was still lower than the changes originating from various cardiovascular diseases (acute myocardial infarction: >128 ms, chronic myocardial infarction: 166 ms, hypertrophic cardiomyopathy: >125 ms, dilated cardiomyopathy: 169 ms, acute viral myocarditis: 154 ms, amyloidosis: >126 ms) (4,59–65), indicating that the proposed technique has the potential for disease detection. The relatively

large CoVs in FF measurement of both reference and VTR Multitasking were caused by low FF values (close to 0) in this cohort.

T1 image quality scores of VTR Multitasking were lower than those of MOLLI but the median score was still “acceptable”. The lower image quality could potentially be explained by the balanced SSFP readouts used in MOLLI, which had higher SNR compared to the GRE readouts used in this work. The proposed VTR Multitasking technique still has unique advantages in resolving motion compared to MOLLI and may therefore benefit patients who cannot breath-hold or for whom ECG triggering fails. We also note that the proposed VTR scheme raised the median T1 image quality from “poor” (for the previous CTR scheme) up to “acceptable”, a critical improvement for clinical application.

Preliminary evaluation of T2* mapping was performed on patients after ferumoxytol administration, which mimicked increased myocardial iron content and resulted in short myocardial T2* values. The results indicated the proposed technique has the potential to detect diffuse T2* changes, e.g., in Thalassemia Major patients. Nevertheless, the range of T1/T2/FF values in the in-vivo study is limited and the patient group has a relatively small size. In the future, more comprehensive patient study with a larger cohort and different disease models should be performed to evaluate the clinical significance of the proposed technique.

At present, standardization of multiparametric myocardial mapping is challenging due to vendor differences in acquisition protocols and post-processing workflow for quantitative cardiovascular MRI. The setup for ECG triggering (acquisition window, trigger delay, etc.) and instructions for breath holding can also vary among MR technologists. In comparison, our proposed method can potentially reduce the vendor-dependence and operator-dependence by introducing a unified protocol and reconstruction scheme, and by removing the need for ECG and breath holding. Future multi-center and multi-vendor studies will be needed for validation. In this work, the technique was implemented and tested on a 3T scanner. In principle, it can also be extended to lower fields (1.5 T or even lower). The main technical challenge would be SNR reduction, as for any other techniques. Balanced SSFP readouts may be incorporated into Multitasking in SNR-demanding scenarios with further technical development.

Another potential area for future improvement is the scan time. Assuming a breath-hold scan plus the recovery period is approximately 1 min, the 2.5 mins needed for our technique is shorter than the 4 mins required for 4 single-parameter scans with reference methods. Nevertheless, it may still be time-consuming if a short-axis stack is desired in a clinical setting. Potential approaches for further acceleration include simultaneous multi-slice acquisition (66) and deep learning based methods such as super-resolution (67). In this study, we only analyzed parametric maps and measurements in the diastolic phase. However, the same parametric maps in systolic phase as well as cine imaging are also readily available with our technique (28). With dynamic information, one can potentially measure the changes of biomarkers throughout the cardiac cycle to reveal physiological information which is currently understudied using conventional techniques. Additionally, with the aid of deep learning reconstruction, inline reconstruction can be implemented (68). Finally, the adoption

of advanced shim-RF coils may potentially reduce B_0 inhomogeneity and susceptibility artifacts in the myocardium especially at high fields (3T and above) (69).

5. Conclusion

A free-breathing, non-ECG technique was developed for simultaneous myocardial T1, T2, T2*, and FF quantification in a single 2.5-min scan based on the MR Multitasking framework. The technique yielded repeatable measurements that agreed with references.

Supplementary Material

Refer to Web version on PubMed Central for supplementary material.

Acknowledgements

This work was partially supported by NIH R01EB028146 and NIH R01HL156818. Dr. Nguyen is supported by NIH R01HL148182 and VA-MERIT I01CX001901. Anthony G. Christodoulou and Debiao Li contributed equally to this work. We acknowledge the use of the Fat-Water Toolbox (http://ismrm.org/workshops/FatWater12/data.htm) for some of the results shown in this article. The authors thank Xinheng Zhang for his help in construction of water/fat phantom. The authors thank Adis Asaturyan, Laura Smith, Irene Lee, and Mike Ngo for their help in coordinating with and scanning the subjects.

References

1. Messroghli DR, Moon JC, Ferreira VM, Grosse-Wortmann L, He T, Kellman P, Mascherbauer J, Nezafat R, Salerno M, Schelbert EB, Taylor AJ, Thompson R, Ugander M, van Heeswijk RB, Friedrich MG. Clinical recommendations for cardiovascular magnetic resonance mapping of T1, T2, T2* and extracellular volume: A consensus statement by the Society for Cardiovascular Magnetic Resonance (SCMR) endorsed by the European Association for Cardiovascular Imaging (EACVI). J Cardiovasc Magn Reson 2017;19(1):75. [PubMed: 28992817]
2. Kim PK, Hong YJ, Im DJ, Suh YJ, Park CH, Kim JY, Chang S, Lee HJ, Hur J, Kim YJ, Choi BW. Myocardial T1 and T2 Mapping: Techniques and Clinical Applications. Korean J Radiol 2017;18(1):113–131. [PubMed: 28096723]
3. Haaf P, Garg P, Messroghli DR, Broadbent DA, Greenwood JP, Plein S. Cardiac T1 Mapping and Extracellular Volume (ECV) in clinical practice: a comprehensive review. J Cardiovasc Magn Reson 2016;18(1):89. [PubMed: 27899132]
4. Puntmann VO, Voigt T, Chen Z, Mayr M, Karim R, Rhode K, Pastor A, Carr-White G, Razavi R, Schaeffter T, Nagel E. Native T1 mapping in differentiation of normal myocardium from diffuse disease in hypertrophic and dilated cardiomyopathy. JACC Cardiovasc Imaging 2013;6(4):475–484. [PubMed: 23498674]
5. Bull S, White SK, Piechnik SK, Flett AS, Ferreira VM, Loudon M, Francis JM, Karamitsos TD, Prendergast BD, Robson MD, Neubauer S, Moon JC, Myerson SG. Human non-contrast T1 values and correlation with histology in diffuse fibrosis. Heart 2013;99(13):932–937. [PubMed: 23349348]
6. Schelbert EB, Messroghli DR. State of the Art: Clinical Applications of Cardiac T1 Mapping. Radiology 2016;278(3):658–676. [PubMed: 26885733]
7. Ugander M, Bagi PS, Oki AJ, Chen B, Hsu LY, Aletras AH, Shah S, Greiser A, Kellman P, Arai AE. Myocardial Edema as Detected by Pre-Contrast T1 and T2 CMR Delineates Area at Risk Associated With Acute Myocardial Infarction. Jacc-Cardiovasc Imag 2012;5(6):596–603.
8. Messroghli DR, Walters K, Plein S, Sparrow P, Friedrich MG, Ridgway JP, Sivananthan MU. Myocardial T-1 mapping: Application to patients with acute and chronic myocardial infarction. Magn Reson Med 2007;58(1):34–40. [PubMed: 17659622]
9. Verhaert D, Thavendiranathan P, Giri S, Mihai G, Rajagopalan S, Simonetti OP, Raman SV. Direct T2 Quantification of Myocardial Edema in Acute Ischemic Injury. Jacc-Cardiovasc Imag 2011;4(3):269–278.

10. Carpenter JP, Roughton M, Pennell DJ, Myocardial Iron in Thalassemia I. International survey of T2* cardiovascular magnetic resonance in beta-thalassemia major. Haematologica 2013;98(9):1368–1374. [PubMed: 23812939]
11. Aydinok Y, Porter JB, Piga A, Elalfy M, El-Beshlawy A, Kilinc Y, Viprakasit V, Yesilipek A, Habr D, Quebe-Fehling E, Pennell DJ. Prevalence and distribution of iron overload in patients with transfusion-dependent anemias differs across geographic regions: results from the CORDELIA study. Eur J Haematol 2015;95(3):244–253. [PubMed: 25418187]
12. Triadyaksa P, Oudkerk M, Sijens PE. Cardiac T2 * mapping: Techniques and clinical applications. J Magn Reson Imaging 2020;52(5):1340–1351. [PubMed: 31837078]
13. Kenchaiah S, Ding J, Carr JJ, Allison MA, Budoff MJ, Tracy RP, Burke GL, McClelland RL, Arai AE, Bluemke DA. Pericardial Fat and the Risk of Heart Failure. J Am Coll Cardiol 2021;77(21):2638–2652. [PubMed: 34045020]
14. Goldfarb JW, Roth M, Han J. Myocardial Fat Deposition after Left Ventricular Myocardial Infarction: Assessment by Using MR Water-Fat Separation Imaging. Radiology 2009;253(1):65–73. [PubMed: 19703860]
15. Kellman P, Hernando D, Arai AE. Myocardial fat imaging. Current cardiovascular imaging reports 2010;3(2):83–91. [PubMed: 20401158]
16. Messroghli DR, Radjenovic A, Kozerke S, Higgins DM, Sivananthan MU, Ridgway JP. Modified Look-Locker inversion recovery (MOLLI) for high-resolution T1 mapping of the heart. Magn Reson Med 2004;52(1):141–146. [PubMed: 15236377]
17. Chow K, Flewitt JA, Green JD, Pagano JJ, Friedrich MG, Thompson RB. Saturation recovery single-shot acquisition (SASHA) for myocardial T(1) mapping. Magn Reson Med 2014;71(6):2082–2095. [PubMed: 23881866]
18. Giri S, Chung YC, Merchant A, Mihai G, Rajagopalan S, Raman SV, Simonetti OP. T2 quantification for improved detection of myocardial edema. J Cardiovasc Magn Reson 2009;11:56. [PubMed: 20042111]
19. Guo R, Chen Z, Wang Y, Herzka DA, Luo J, Ding H. Three-dimensional free breathing whole heart cardiovascular magnetic resonance T1 mapping at 3 T. J Cardiovasc Magn Reson 2018;20(1):64. [PubMed: 30220254]
20. van Heeswijk RB, Feliciano H, Bongard C, Bonanno G, Coppo S, Lauriers N, Locca D, Schwitter J, Stuber M. Free-breathing 3 T magnetic resonance T2-mapping of the heart. JACC Cardiovasc Imaging 2012;5(12):1231–1239. [PubMed: 23236973]
21. Hermann I, Kellman P, Demirel OB, Akcakaya M, Schad LR, Weingartner S. Free-breathing simultaneous T 1, T 2, and T 2 * quantification in the myocardium. Magn Reson Med 2021;86(3):1226–1240. [PubMed: 33780037]
22. Cruz G, Jaubert O, Qi H, Bustin A, Milotta G, Schneider T, Koken P, Doneva M, Botnar RM, Prieto C. 3D free-breathing cardiac magnetic resonance fingerprinting. NMR Biomed 2020;33(10):e4370. [PubMed: 32696590]
23. Qi H, Bustin A, Cruz G, Jaubert O, Chen H, Botnar RM, Prieto C. Free-running simultaneous myocardial T1/T2 mapping and cine imaging with 3D whole-heart coverage and isotropic spatial resolution. Magn Reson Imaging 2019;63:159–169. [PubMed: 31425810]
24. Qi H, Jaubert O, Bustin A, Cruz G, Chen H, Botnar R, Prieto C. Free-running 3D whole heart myocardial T1 mapping with isotropic spatial resolution. Magn Reson Med 2019;82(4):1331–1342. [PubMed: 31099442]
25. Santelli C, Nezafat R, Goddu B, Manning WJ, Smink J, Kozerke S, Peters DC. Respiratory bellows revisited for motion compensation: preliminary experience for cardiovascular MR. Magn Reson Med 2011;65(4):1097–1102. [PubMed: 21413074]
26. Krug J, Rose G, Stucht D, Clifford G, Oster J. Limitations of VCG based gating methods in ultra high field cardiac MRI. Journal of Cardiovascular Magnetic Resonance 2013;15(1):1–2. [PubMed: 23324167]
27. Nacif MS, Zavodni A, Kawel N, Choi EY, Lima JA, Bluemke DA. Cardiac magnetic resonance imaging and its electrocardiographs (ECG): tips and tricks. Int J Cardiovasc Imaging 2012;28(6):1465–1475. [PubMed: 22033762]

28. Christodoulou AG, Shaw JL, Nguyen C, Yang Q, Xie YB, Wang N, Li DB. Magnetic resonance multitasking for motion-resolved quantitative cardiovascular imaging. Nat Biomed Eng 2018;2(4):215–226. [PubMed: 30237910]
29. Shaw JL, Yang Q, Zhou ZW, Deng ZX, Nguyen C, Li DB, Christodoulou AG. Free-breathing, non-ECG, continuous myocardial T-1 mapping with cardiovascular magnetic resonance multitasking. Magn Reson Med 2019;81(4):2450–2463. [PubMed: 30450749]
30. Cao T, Ma S, Wang N, Gharabaghi S, Xie Y, Fan Z, Hogg E, Wu C, Han F, Tagliati M, Haacke EM, Christodoulou AG, Li D. Three-dimensional simultaneous brain mapping of T1, T2, T2* and magnetic susceptibility with MR Multitasking. Magn Reson Med 2021.
31. Wang N, Cao T, Han F, Xie Y, Zhong X, Ma S, Kwan A, Fan Z, Han H, Bi X, Noureddin M, Deshpande V, Christodoulou AG, Li D. Free-breathing multitasking multi-echo MRI for whole-liver water-specific T1, proton density fat fraction, and R2* quantification. Magn Reson Med 2021.
32. Hernando D, Kellman P, Haldar JP, Liang ZP. Robust Water/Fat Separation in the Presence of Large Field Inhomogeneities Using a Graph Cut Algorithm. Magn Reson Med 2010;63(1):79–90. [PubMed: 19859956]
33. Liang Z-P. Spatiotemporal imaging with partially separable functions. Proc IEEE Int Symp Biomed Imaging 2007:988–991.
34. He J, Liu Q, Christodoulou AG, Ma C, Lam F, Liang Z-P. Accelerated high-dimensional MR imaging with sparse sampling using low-rank tensors. IEEE Trans Med Imaging 2016;35(9):2119–2129. [PubMed: 27093543]
35. Kolda TG, Bader BW. Tensor Decompositions and Applications. Siam Rev 2009;51(3):455–500.
36. Tucker LR. Some mathematical notes on three-mode factor analysis. Psychometrika 1966;31(3):279–311. [PubMed: 5221127]
37. Hu Z, Christodoulou AG, Wang N, Shaw JL, Song SS, Maya MM, Ishimori ML, Forbess LJ, Xiao J, Bi X, Han F, Li D, Fan Z. Magnetic resonance multitasking for multidimensional assessment of cardiovascular system: Development and feasibility study on the thoracic aorta. Magn Reson Med 2020;84(5):2376–2388. [PubMed: 32301164]
38. Wang N, Gaddam S, Wang L, Xie Y, Fan Z, Yang W, Tuli R, Lo S, Hendifar A, Pandol S, Christodoulou AG, Li D. Six-dimensional quantitative DCE MR Multitasking of the entire abdomen: Method and application to pancreatic ductal adenocarcinoma. Magn Reson Med 2020;84(2):928–948. [PubMed: 31961967]
39. De Lathauwer L, De Moor B, Vandewalle J. A multilinear singular value decomposition. SIAM journal on Matrix Analysis and Applications 2000;21(4):1253–1278.
40. Yu HZ, Shimakawa A, McKenzie CA, Brodsky E, Brittain JH, Reeder SB. Multiecho Water-Fat Separation and Simultaneous R-2* Estimation With Multifrequency Fat Spectrum Modeling. Magn Reson Med 2008;60(5):1122–1134. [PubMed: 18956464]
41. Liu CY, McKenzie CA, Yu H, Brittain JH, Reeder SB. Fat quantification with IDEAL gradient echo imaging: Correction of bias from T-1 and noise. Magn Reson Med 2007;58(2):354–364. [PubMed: 17654578]
42. Roy C, Slimani A, de Meester C, Amzulescu M, Pasquet A, Vancraeynest D, Vanoverschelde JL, Pouleur AC, Gerber BL. Age and sex corrected normal reference values of T1, T2 T2* and ECV in healthy subjects at 3T CMR. J Cardiovasc Magn Reson 2017;19(1):72. [PubMed: 28934962]
43. Jaubert O, Cruz G, Bustin A, Schneider T, Lavin B, Koken P, Hajhosseiny R, Doneva M, Rueckert D, Botnar RM, Prieto C. Water-fat Dixon cardiac magnetic resonance fingerprinting. Magn Reson Med 2020;83(6):2107–2123. [PubMed: 31736146]
44. Idilman IS, Aniktar H, Idilman R, Kabacam G, Savas B, Elhan A, Celik A, Bahar K, Karcaaltincaba M. Hepatic steatosis: quantification by proton density fat fraction with MR imaging versus liver biopsy. Radiology 2013;267(3):767–775. [PubMed: 23382293]
45. Procter AJ, Sun JY, Malcolm PN, Toms AP. Measuring liver fat fraction with complex-based chemical shift MRI: the effect of simplified sampling protocols on accuracy. BMC Med Imaging 2019;19(1):14. [PubMed: 30736759]

46. Yu H, McKenzie CA, Shimakawa A, Vu AT, Brau AC, Beatty PJ, Pineda AR, Brittain JH, Reeder SB. Multiecho reconstruction for simultaneous water-fat decomposition and T2* estimation. J Magn Reson Imaging 2007;26(4):1153–1161. [PubMed: 17896369]
47. Alam MH, Auger D, McGill LA, Smith GC, He T, Izgi C, Baksi AJ, Wage R, Drivas P, Firmin DN, Pennell DJ. Comparison of 3 T and 1.5 T for T2* magnetic resonance of tissue iron. J Cardiovasc Magn Reson 2016;18(1):40. [PubMed: 27391316]
48. Cerqueira MD, Weissman NJ, Dilsizian V, Jacobs AK, Kaul S, Laskey WK, Pennell DJ, Rumberger JA, Ryan T, Verani MS, Grp AHAW. Standardized myocardial segmentation and nomenclature for tomographic imaging of the heart - A statement for healthcare professionals from the Cardiac Imaging Committee of the Council on Clinical Cardiology of the American Heart Association. Circulation 2002;105(4):539–542. [PubMed: 11815441]
49. da Cruz GJL, Velasco C, Lavin B, Jaubert O, Botnar RM, Prieto C. Myocardial T1, T2, T2*, and fat fraction quantification via low-rank motion-corrected cardiac MR fingerprinting. Magn Reson Med 2022.
50. Sievers B, Wiesner M, Kiria N, Speiser U, Schoen S, Strasser RH. Influence of the trigger technique on ventricular function measurements using 3-Tesla magnetic resonance imaging: comparison of ECG versus pulse wave triggering. Acta Radiol 2011;52(4):385–392. [PubMed: 21498278]
51. Kellman P, Hansen MS. T1-mapping in the heart: accuracy and precision. J Cardiovasc Magn Reson 2014;16:2. [PubMed: 24387626]
52. Jiang Y, Ma D, Keenan KE, Stupic KF, Gulani V, Griswold MA. Repeatability of magnetic resonance fingerprinting T1 and T2 estimates assessed using the ISMRM/NIST MRI system phantom. Magn Reson Med 2017;78(4):1452–1457. [PubMed: 27790751]
53. Meloni A, Positano V, Keilberg P, De Marchi D, Pepe P, Zuccarelli A, Campisi S, Romeo MA, Casini T, Bitti PP, Gerardi C, Lai ME, Piraino B, Giuffrida G, Secchi G, Midiri M, Lombardi M, Pepe A. Feasibility, reproducibility, and reliability for the T*2 iron evaluation at 3 T in comparison with 1.5 T. Magn Reson Med 2012;68(2):543–551. [PubMed: 22127999]
54. Reeder SB, Faranesh AZ, Boxerman JL, McVeigh ER. In vivo measurement of T* 2 and field inhomogeneity maps in the human heart at 1.5 T. Magn Reson Med 1998;39(6):988–998. [PubMed: 9621923]
55. Fischer K, Yamaji K, Luescher S, Ueki Y, Jung B, von Tengg-Kobligk H, Windecker S, Friedrich MG, Eberle B, Guensch DP. Feasibility of cardiovascular magnetic resonance to detect oxygenation deficits in patients with multi-vessel coronary artery disease triggered by breathing maneuvers. Journal of Cardiovascular Magnetic Resonance 2018;20. [PubMed: 29544514]
56. Gottbircht M, Kramer CM, Salerno M. Native T1 and Extracellular Volume Measurements by Cardiac MRI in Healthy Adults: A Meta-Analysis. Radiology 2019;290(2):317–326. [PubMed: 30422092]
57. Liu CY, Redheuil A, Ouwerkerk R, Lima JA, Bluemke DA. Myocardial fat quantification in humans: Evaluation by two-point water-fat imaging and localized proton spectroscopy. Magn Reson Med 2010;63(4):892–901. [PubMed: 20373390]
58. von Knobelsdorff-Brenkenhoff F, Prothmann M, Dieringer MA, Wassmuth R, Greiser A, Schwenke C, Niendorf T, Schulz-Menger J. Myocardial T-1 and T-2 mapping at 3 T: reference values, influencing factors and implications. Journal of Cardiovascular Magnetic Resonance 2013;15. [PubMed: 23343426]
59. Puntmann VO, Peker E, Chandrashekhar Y, Nagel E. T1 Mapping in Characterizing Myocardial Disease A Comprehensive Review. Circ Res 2016;119(2):277–299. [PubMed: 27390332]
60. Messroghli DR, Niendorf T, Schulz-Menger J, Dietz R, Friedrich MG. T1 mapping in patients with acute myocardial infarction. J Cardiovasc Magn Reson 2003;5(2):353–359. [PubMed: 12765114]
61. Dastidar AG, Harries I, Pontecorboli G, Bruno VD, De Garate E, Moret C, Baritussio A, Johnson TW, McAlindon E, Bucciarelli-Ducci C. Native T1 mapping to detect extent of acute and chronic myocardial infarction: comparison with late gadolinium enhancement technique. Int J Cardiovas Imag 2019;35(3):517–527.
62. Hinojar R, Varma N, Child N, Goodman B, Jabbour A, Yu CY, Gebker R, Doltra A, Kelle S, Khan S, Rogers T, Ucar EA, Cummins C, Carr-White G, Nagel E, Puntmann VO. T1 Mapping

in Discrimination of Hypertrophic Phenotypes: Hypertensive Heart Disease and Hypertrophic Cardiomyopathy Findings From the International T1 Multicenter Cardiovascular Magnetic Resonance Study. Circ-Cardiovasc Imag 2015;8(12).

63. Hinojar R, Puntmann VO. Native T1 in Discrimination of Acute and Convalescent Stages in Patients With Clinical Diagnosis of Myocarditis A Proposed Diagnostic Algorithm Using CMR. Jacc-Cardiovasc Imag 2015;8(1):38–46.
64. Fontana M, Banypersad SM, Treibel TA, Maestrini V, Sado DM, White SK, Pica S, Castelletti S, Piechnik SK, Robson MD, Gilbertson JA, Rowczenio D, Hutt DF, Lachmann HJ, Wechalekar AD, Whelan CJ, Gillmore JD, Hawkins PN, Moon JC. Native T1 Mapping in Transthyretin Amyloidosis. Jacc-Cardiovasc Imag 2014;7(2):157–165.
65. Banypersad SM, Fontana M, Maestrini V, Sado DM, Captur G, Petrie A, Piechnik SK, Whelan CJ, Herrey AS, Gillmore JD, Lachmann HJ, Wechalekar AD, Hawkins PN, Moon JC. T1 mapping and survival in systemic light-chain amyloidosis. Eur Heart J 2015;36(4):244–251. [PubMed: 25411195]
66. Mao X, Lee H, Ma S, Hu Z, Han F, Xie Y, Li D, Christodoulou AG. Simultaneous Multi-slice Cardiac MR Multitasking for Motion-Resolved, Non-ECG, Free-Breathing Joint T1-T2 Mapping. 2021; An Online Experiene.
67. Chen Y, Shi F, Christodoulou AG, Xie Y, Zhou Z, Li D. Efficient and accurate MRI super-resolution using a Generative Adversarial Network and 3D Multi-level Densely Connected Network. Med Image Comput Comput Assist Interv 2018:91–99.
68. Chen Y, Shaw JL, Xie Y, Li D, Christodoulou AG. Deep learning within *a priori* temporal feature spaces for large-scale dynamic MR image reconstruction: Application to 5-D cardiac MR Multitasking. Med Image Comput Comput Assist Interv 2019;11765:495–504. [PubMed: 31723946]
69. Han H, Song AW, Truong TK. Integrated parallel reception, excitation, and shimming (iPRES). Magn Reson Med 2013;70(1):241–247. [PubMed: 23629974]

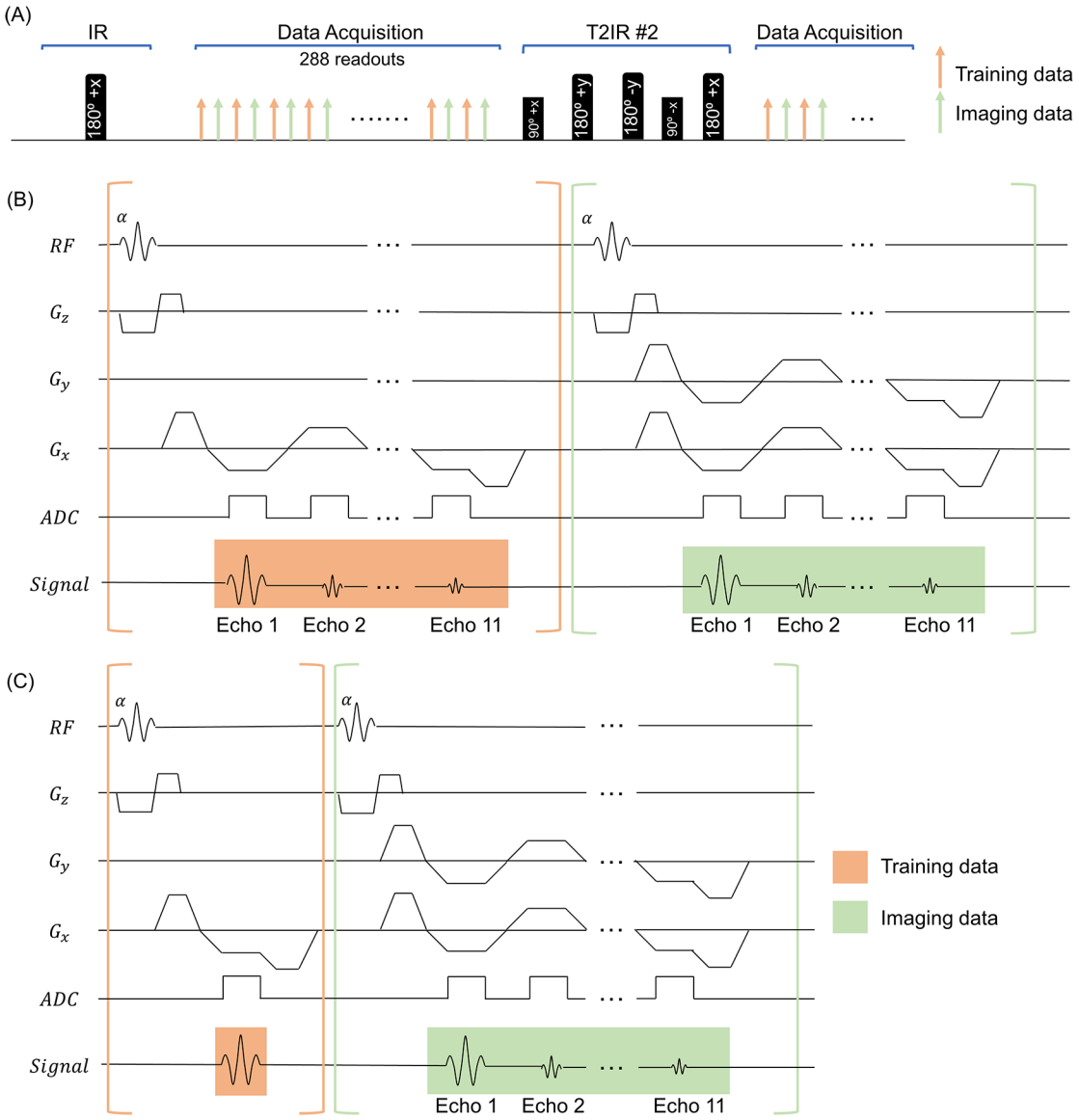

Figure 1.

(A) Sequence diagram for the proposed multitasking T1/T2/T2*/FF mapping framework. Hybrid IR/T2IR preparation modules were followed by 288 FLASH readouts, which enable collection of k-space lines with different T1/T2/T2* contrasts. The training data was acquired every other readout.

(B) Illustration of constant T_R (CTR) readout module, which used multi-echo readouts for both training and imaging data.

(C) Illustration of variable T_R (VTR) readout module, which used a single-echo readout for training data and multi-echo readouts for imaging data

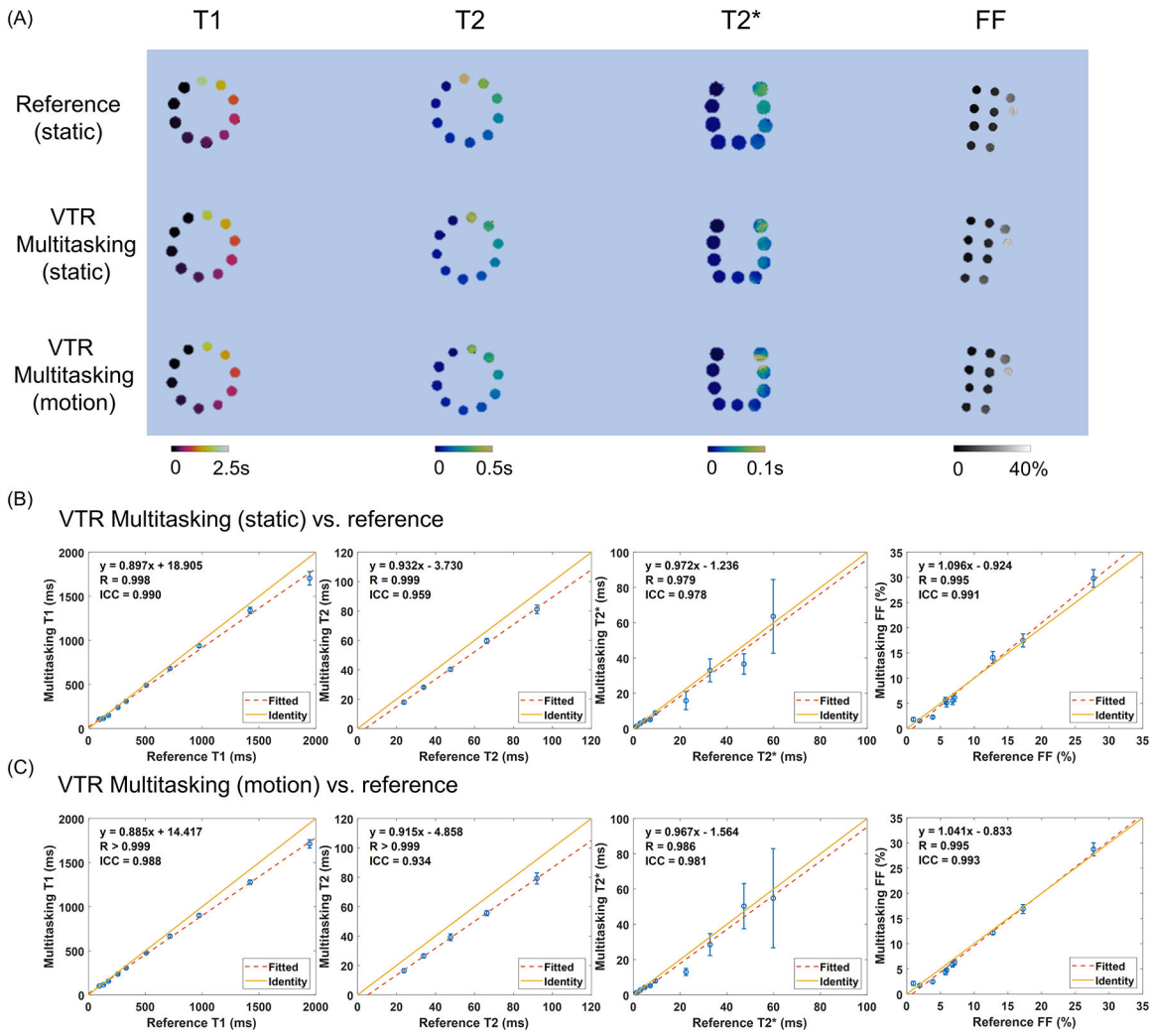

Figure 2.

(A) Reference maps (1st row), VTR Multitasking maps collected without motion (2nd row), and VTR Multitasking maps collected with motion (3rd row) for NIST, Calimetrix, and FF phantoms.

(B) The correlation plot between VTR Multitasking measurements (collected without motion) and reference measurements, with correlation coefficients and ICCs labeled ($R > 0.97$, $ICC > 0.95$).

(C) The correlation plot between VTR Multitasking measurements (collected with motion) and reference measurements, with correlation coefficients and ICCs labeled ($R > 0.98$, $ICC > 0.93$).

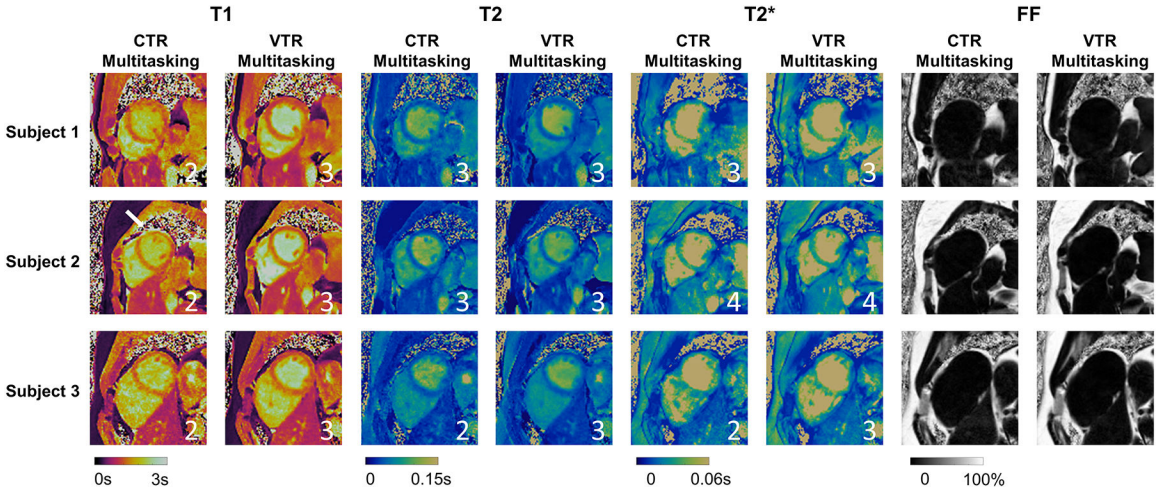

Figure 3.

Comparison of T1, T2, T2*, and FF maps between VTR Multitasking and CTR Multitasking method on three representative healthy subjects. The image quality scores from the cardiologist were labelled at the bottom-right corner of corresponding maps.

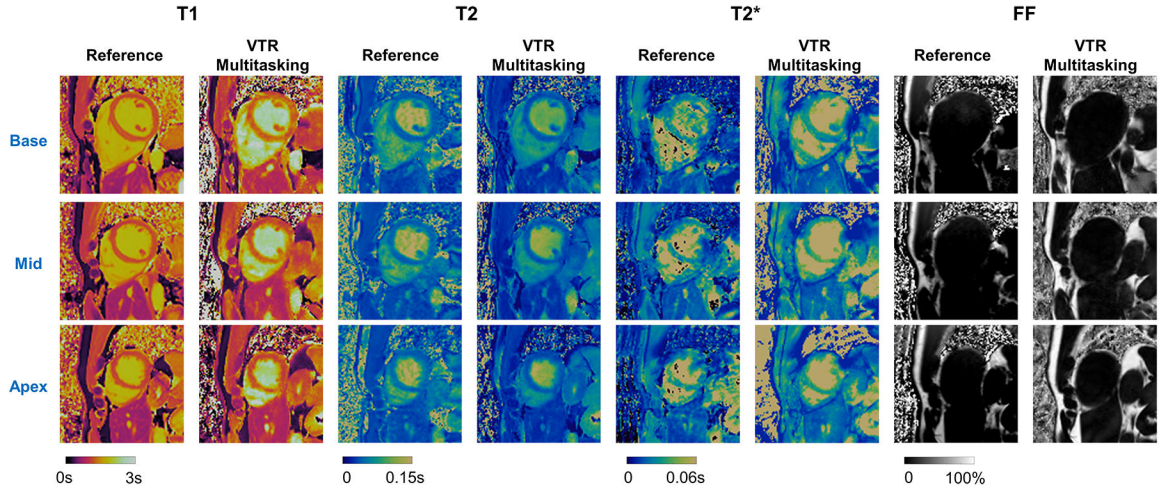

Figure 4.

T1, T2, T2*, and FF maps from VTR Multitasking and references on a representative healthy subject. The image quality scores for the mid-ventricular slice were: reference T1 – 4 (excellent); reference T2 – 3 (acceptable); reference T2* - 3 (good); VTR Multitasking T1 – 3 (acceptable); VTR Multitasking T2 – 3 (acceptable); VTR Multitasking T2* - 3 (good).

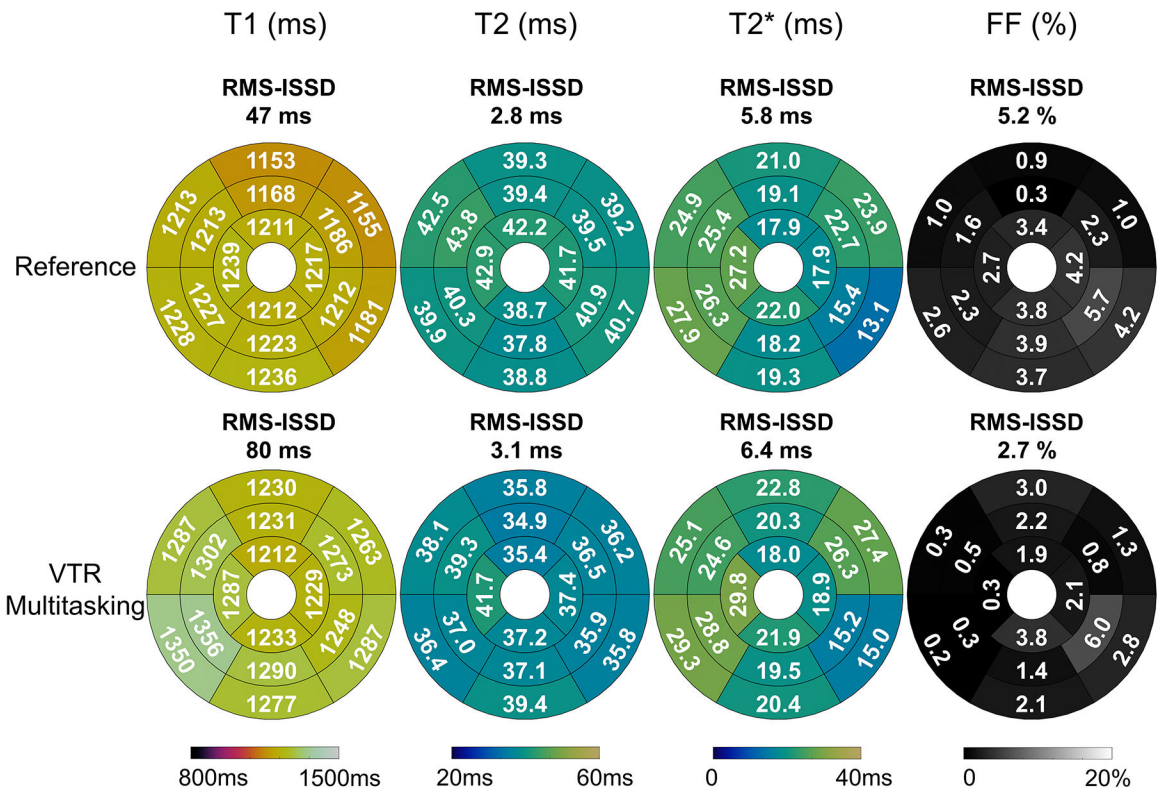

Figure 5.

Bullseye plot of average T1, T2, T2*, and FF measurements in healthy subjects (N=12) acquired with VTR Multitasking and references, with RMS-ISSD labelled to indicate the spatial variability.

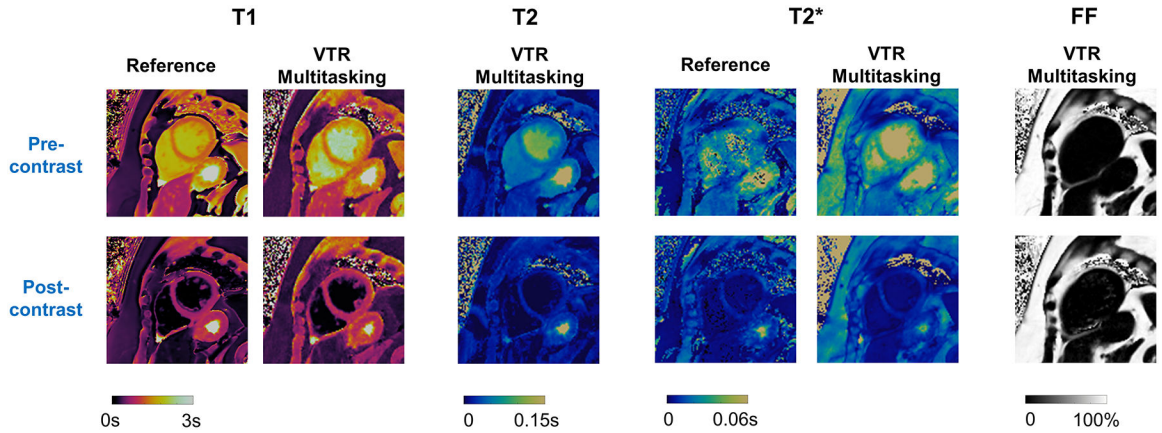

Figure 6.
VTR Multitasking maps and available reference maps on a 66-year-old patient pre- and post-ferumoxytol administration.

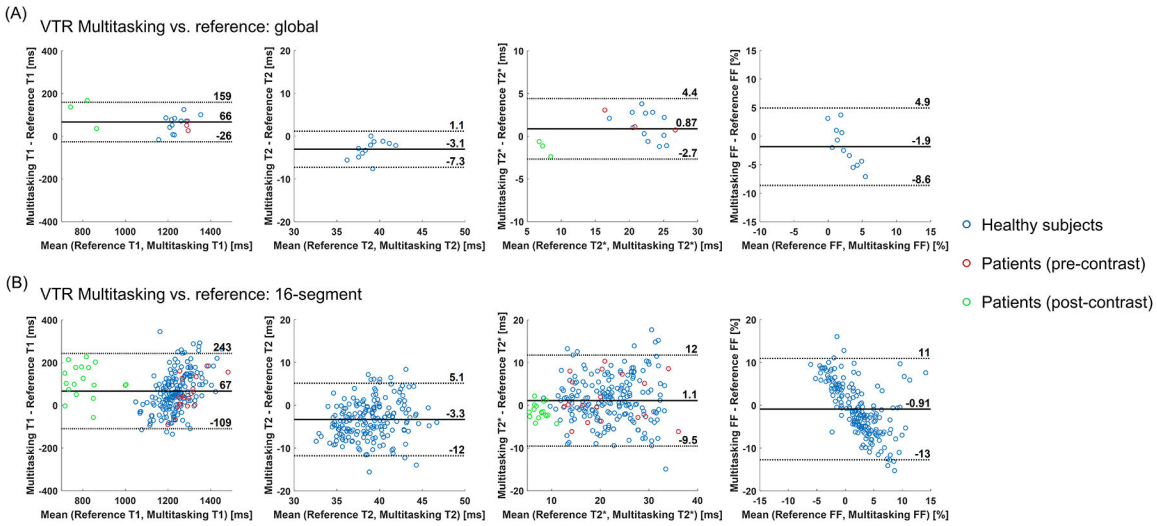

Figure 7.

Bland-Altman plots comparing T1, T2, T2*, and FF measurements from references and Multitasking techniques in global myocardium (A) and in all 16 segments (B). The dotted lines indicate the 95% limits of agreement and the solid lines indicate mean bias.

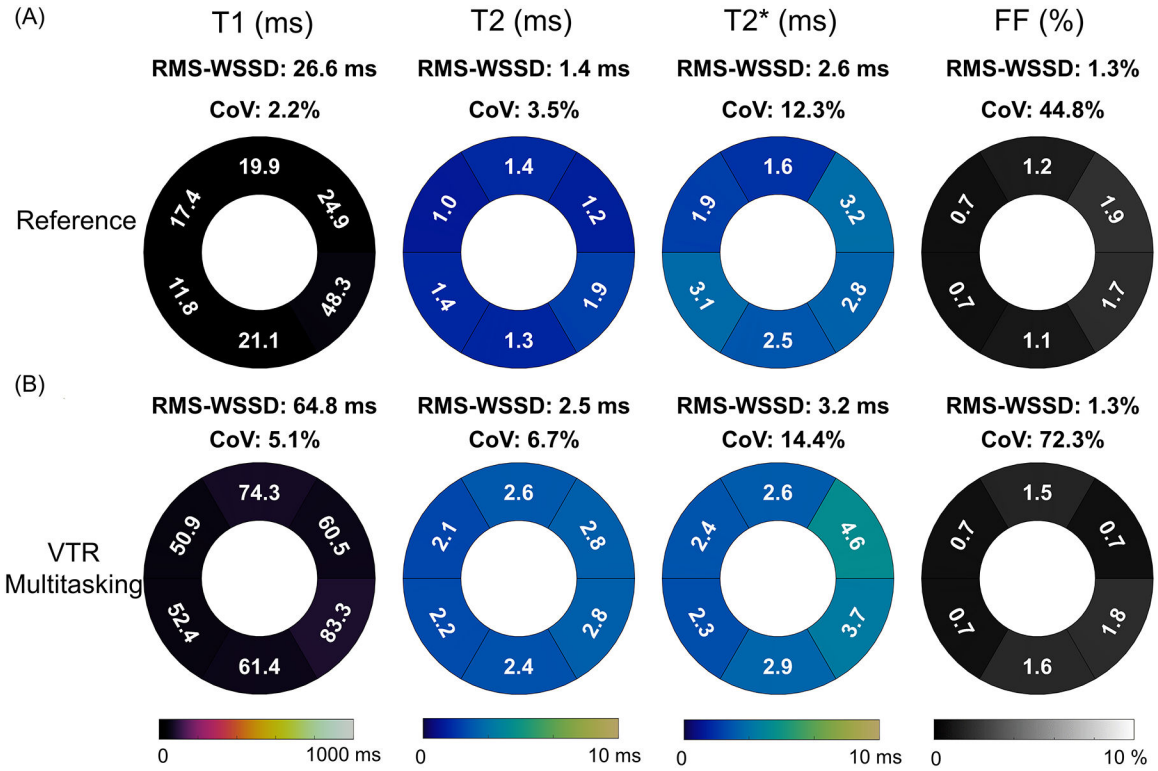

Figure 8.

Reference (A) and Multitasking (B) measurement repeatability. Both methods demonstrated good repeatability, as indicated by RMS-WSSD and CoV.

Table 1.

VTR Multitasking T1/T2/T2*/FF mapping protocol. Recovery period refers to the spacing between preparation pulses.

FOV (mm)	270	Phase FOV	100%
Scanning matrix	160 × 160	Slice thickness (mm)	8.0
Resolution (mm)	1.7 × 1.7	Number of readout modules per shot	288
Recovery period (ms)	2900	Echo time (ms)	1.6 – 14.6 (11 echoes)
Imaging data T_R (ms)	16.6	Training data T_R (ms)	3.6
T2IR prep duration (ms)	0, 30, 40, 50, 60	Pixel BW (Hz/pixel)	1008
Flip angle (°)	5	Scan time per slice (min:sec)	2:31
Acquisition	2D single slice	Sampling trajectory	Golden Angle Radial
Reconstruction time (h)	3.5		

Table 2.

VTR Multitasking and reference measurements for all subjects.

		Reference	VTR Multitasking
Healthy volunteers (N=12)	T1 (ms)	1207.8 ± 41.8	1266.8 ± 65.8
	T2 (ms)	40.5 ± 1.4	37.4 ± 2.3
	T2* (ms)	21.9 ± 2.9	23.2 ± 2.2
	FF (%)	2.7 ± 3.5	1.6 ± 1.0
Patients (pre-contrast, N=3)	T1 (ms)	1266.6 ± 10.6	1316.1 ± 8.3
	T2* (ms)	20.5 ± 4.7	22.1 ± 3.8
Patients (post-contrast, N=3)	T1 (ms)	752.5 ± 71.2	866.0 ± 39.8
	T2* (ms)	8.2 ± 1.1	6.8 ± 0.3